

High-Resolution Retrieval of Atmospheric Boundary Layers with Nonstationary Gaussian Processes

Haoran Xiong^{*†} Paytsar Muradyan[‡] Christopher J. Geoga[†]

Abstract

The atmospheric boundary layer (ABL) plays a critical role in governing turbulent exchanges of momentum, heat moisture, and trace gases between the Earth’s surface and the free atmosphere, thereby influencing meteorological phenomena, air quality, and climate processes. Accurate and temporally continuous characterization of the ABL structure and height evolution is crucial for both scientific understanding and practical applications. High-resolution retrievals of the ABL height from vertical velocity measurements is challenging because it is often estimated using empirical thresholds applied to profiles of vertical velocity variance or related turbulence diagnostics at each measurement altitude, which can suffer from limited sampling and sensitivity to noise. To address these limitations, this work employs nonstationary Gaussian process (GP) modeling to more effectively capture the spatio-temporal dependence structure in the data, enabling high-quality—and, if desired, high-resolution—estimates of the ABL height without reliance on ad-hoc parameter tuning. By leveraging Vecchia approximations, the proposed method can be applied to large-scale datasets, and example applications using full-day vertical velocity profiles comprising approximately 5M measurements are presented.

Keywords: Meteorology, spatio-temporal analysis, Vecchia approximation

^{*}Corresponding author: haoran.xiong@wisc.edu

[†]Department of Statistics, University of Wisconsin-Madison

[‡]Environmental Science Division, Argonne National Laboratory

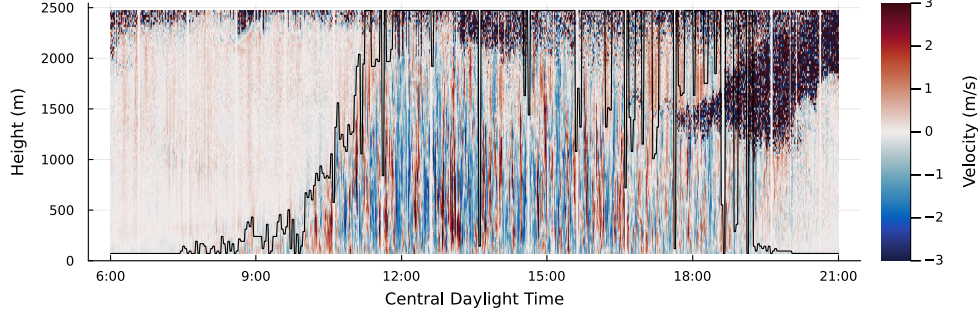
1 Introduction

The atmospheric boundary layer (ABL), also known as the planetary boundary layer (PBL), forms the lowest part of the atmosphere and is directly influenced by surface processes such as momentum flux, sensible and latent heat exchange, and surface radiative and moisture variations (Garratt, 1994; Stull, 2012). Its depth typically ranges from several hundred meters to a few kilometers, depending on the time of day, surface characteristics, and synoptic conditions. During daytime, solar radiation heats the surface, enhancing buoyant convection and turbulence, which deepen the ABL. At night, radiative cooling and reduced turbulent mixing produce a stably stratified and shallow ABL (Mahrt, 2014; Stull, 2012). Capturing these diurnal and synoptic-scale variations is crucial for weather forecasting, air-quality assessment (Dabberdt et al., 2004; Holtslag & Boville, 1993), and climate studies (Baklanov et al., 2014; Holtslag et al., 2013).

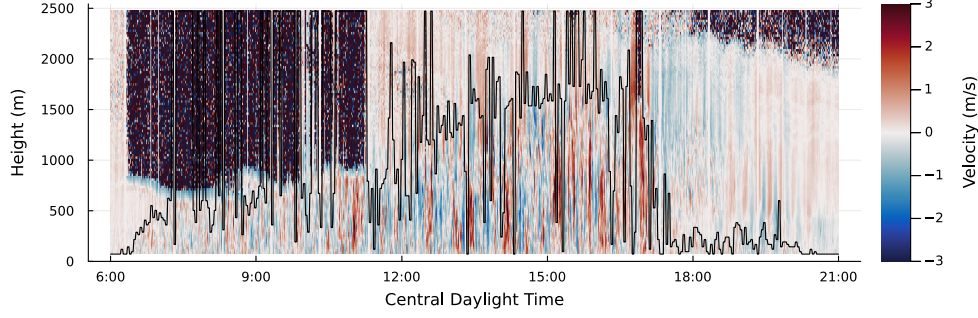
A common challenge in ABL research is to estimate the ABL height using remote-sensing observations such as Doppler Lidar (DL) (Geoga et al., 2021; Pearson et al., 2009; Tucker et al., 2009; F. Wang et al., 2021), micropulse LIDAR (Dang et al., 2019; Y. Wang et al., 2021), or ceilometer backscatter profiles (Eresmaa et al., 2006; Kotthaus et al., 2020). For DLs, the ABL height is often inferred from vertical velocity variance or spectral width profiles, which serve as proxies for turbulence intensity. Current methods involve dividing the data into fixed time segments at each altitude, computing marginal variances while assuming temporal independence, and applying empirical thresholds to identify the transition from turbulent (mixed-layer) to laminar (free-atmosphere) regimes (Tucker et al., 2009). These traditional variance-threshold methods, however, have inherent limitations arising from the intermittent nature of atmospheric turbulence. Because turbulent motions are highly variable in space and time, segments of low-variance can occur within the ABL, while elevated variance values may also appear above it, particularly in the presence of cloud layers, shear zones, or residual-layer turbulence. This intermittency and overlap between regimes can lead to substantial retrieval uncertainty and frequent misidentification of the true ABL top. Ignoring temporal and spatial dependence also introduces bias-variance tradeoffs, which becomes particularly problematic under rapidly evolving ABL conditions. Moreover, a single universal variance threshold rarely performs consistently across different atmospheric stability regimes, cloud cover, or time of day, limiting automation of long-term retrieval without manual tuning.

To illustrate these challenges, Figure 1 shows an example ABL height estimation based on a variance threshold for three different days under different cloud conditions. In this example, the variance is calculated over windows of 300 samples that last approximately 160 seconds each, and a variance threshold of $0.04 \text{ m}^2 \cdot \text{s}^{-2}$, following Tucker et al. (2009), was applied. The dark regions at higher altitudes correspond to low signal-to-noise ratio (SNR) and cloud contamination or blockage, where DL returns are unreliable. As is clear from visual inspection, this threshold-based estimate fluctuates considerably. While temporal smoothing could reduce this variability, it would further degrade temporal resolution of the estimator, reducing the ability to resolve rapid features in the boundary-layer transition.

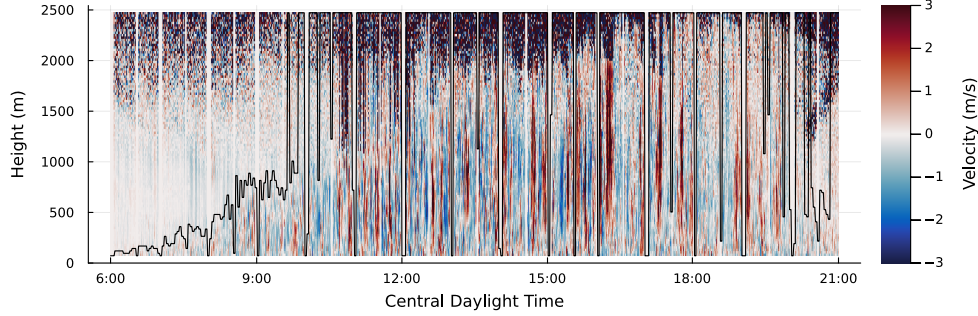
In this work, we propose an alternative approach using nonstationary Gaussian processes (GPs) models specifically designed to capture the strong spatio-temporal correlations inherent in vertical velocity measurements, which can be used to identify local changes of the ABL height. The key idea



(a) The ABL height estimation for June 23, 2023.



(b) The ABL height estimation for June 27, 2023.



(c) The ABL height estimation for July 20, 2023.

Figure 1: The ABL height estimation for three days with variance threshold $0.04 \text{ m}^2 \cdot \text{s}^{-2}$.

of our formulation is that a time-varying ABL height is embedded within the covariance function of the GP, so that the maximum likelihood estimation of the covariance parameters simultaneously yields the ABL height. By explicitly modeling cross-time and cross-height dependencies, the GP model extracts more information than a marginal variance-based approach and significantly mitigates the disadvantage of missing the correlation between contiguous time segments. Moreover, it enables continuous, high temporal resolution retrievals, approaching the native measurement frequency, and provides data-driven differentiation between turbulent and non-turbulent layers, eliminating the need for ad-hoc variance thresholds.

The remainder of this paper is structured as follows. Section 2 introduces the proposed methodology, detailing model assumptions, formulations, and computational framework. Section 3, presents results from three representative case studies under distinct cloud conditions. Finally,

Section 4 discusses implications of our findings and outlines potential directions for future research.

2 Methodology

2.1 Gaussian processes

A Gaussian process (GP) is a stochastic process where every finite set of random variables follows a multivariate Gaussian distribution. The process is typically indexed by time or space and thus suitable for modeling in many environmental applications, including wind profiles. Since a multivariate Gaussian distribution only depends on its mean vector and covariance matrix, a GP is uniquely determined by its mean and covariance function, making it one of the easiest multivariate laws to fully specify. Practitioners often assume a zero mean, use a parametric covariance function, and estimate its parameters from a collection of observations. Specifically, the distribution of n observations $\mathbf{y} = \{y_j\}_{j=1}^n$ at different locations $\{\mathbf{x}_j\}_{j=1}^n$ is $\mathcal{N}(\mathbf{0}, \Sigma)$, where Σ is the covariance matrix induced by the covariance function $K(\cdot, \cdot | \boldsymbol{\theta})$ with a parameter vector $\boldsymbol{\theta}$ such that $\Sigma_{j,k} = K(\mathbf{x}_j, \mathbf{x}_k | \boldsymbol{\theta})$. A common choice for estimating $\boldsymbol{\theta}$ is the maximum likelihood estimator (MLE), which is the vector $\hat{\boldsymbol{\theta}}$ that maximizes the likelihood. For the convenience of optimization, people usually consider minimizing the negative log-likelihood

$$-\ell(\boldsymbol{\theta}) = \frac{n}{2} \log(2\pi) + \frac{1}{2} \log |\Sigma(\boldsymbol{\theta})| + \frac{1}{2} \mathbf{y}^T \Sigma(\boldsymbol{\theta})^{-1} \mathbf{y}, \quad (1)$$

where $|\Sigma(\boldsymbol{\theta})|$ denotes the determinant of $\Sigma(\boldsymbol{\theta})$. One of the several significant conveniences of GP models is that conditional expectations are linear transformations of the data and conditional distributions are themselves Gaussian, making prediction and uncertainty quantification simple and interpretable. They are also extremely flexible interpolators because the choice of covariance function has a significant impact on the behavior and implied conditional distributions of predictions (Stein, 1999). By choosing one covariance function over another, one can effectively determine the correlation length scale, (local) anisotropy, mean-square differentiability (including fractional levels), and more.

In this work in particular, the GP model will use the fact that local behavior above and in the ABL differs in several important ways. Inspection of Figure 1 shows several immediate local properties that change sharply with altitude: the spatial dependence length scale is significantly higher above the ABL, and the temporal roughness and marginal variance is materially higher in the ABL versus above it. More subtle instrument artifacts can also be observed, such as higher measurement noise at higher altitudes. Encoding these physical and measurement characteristics into the covariance function of a GP model will mean that they can be utilized to accurately distinguish measurements that are in the ABL versus above it.

As is common for contemporary datasets and problems, there are two challenges to this GP application that require discussion: model design and computation. It is clear that using an off-the-shelf covariance function will not be possible for this application, and building a covariance function that has been specifically designed to be fit-for-purpose will be necessary. The second issue is even more universal: the computation of (1) involves calculating a determinant and solving a linear system, which for a dense $\Sigma(\boldsymbol{\theta})$ is most effectively done with a Cholesky factorization

that requires $\mathcal{O}(n^3)$ work and $\mathcal{O}(n^2)$ storage. For reference, this work will be applied to full-day profiles that contain approximately 5M measurements. A square matrix of edge length 5M would require approximately 182 terabytes of RAM to store, and would obviously require an unacceptable amount of time to factorize even once—let alone hundreds of times as would naturally be required in the process of using an optimizer to compute an MLE. We will discuss design choices to address both of these issues in the next two sections.

2.2 A GP model for DL vertical velocity profiles

In the particular case of DL vertical velocity profiles, we adopt a nonstationary GP model formulated as a mixture of two dependent (locally) stationary components representing the turbulent (in-ABL) and laminar (above-ABL) regimes. This formulation extends the mixture-of-stationary nonstationary modeling framework of Fuentes and Smith (2001) to allow for explicit dependence between the two regimes and smooth temporal variations of their relative influence. Specifically, within time intervals over which the in-ABL and above-ABL dynamics can each be considered approximately stationary, we consider the model

$$Z(t, x) = (1 - w(t, x))Z_1(t, x) + w(t, x)Z_2(t, x), \quad (2)$$

which can be treated as a convex combination of the two components of a bivariate stationary Gaussian process with components denoted Z_1 and Z_2 that represent the processes in and above the ABL respectively. The function $w(t, x) \in (0, 1)$ here encodes information about the ABL height, up- or down-weighting one term or the other in the process depending on whether a given altitude x is above the ABL or not. In particular, we use the simple parameterization of

$$w(t, x) = \frac{1}{1 + \exp\{-s(x - \alpha(t))\}}, \quad (3)$$

where $\alpha(t)$ is the ABL height at time t , and s is the parameter adjusting the transition rate between Z_1 and Z_2 . When the point (t, x) lies well below the ABL height, $w(t, x)$ is close to 0, and Z_1 is the dominant term in Z . When the point (t, x) lies well above the ABL, $w(t, x)$ is close to 1, and Z_2 is dominant in Z . The ABL height $\alpha(t)$ is parameterized as

$$\alpha(t) = \sum_{j=1}^m c_j \psi_j(t), \quad (4)$$

where $\psi_j(t)$'s are local basis functions that can be placed as finely or coarsely as desired for the specific application. In the next section, we will demonstrate two different designs for $\alpha(t)$; one, based on wavelets, is ideal for high-resolution estimation of the ABL height. The other, based on splines, is useful at coarser timescales for producing full-day profiles of the ABL, including in the presence of gaps and other irregularities in the data.

Using the multivariate Matérn model of (Gneiting et al., 2010), the marginal covariance functions for Z_1 and Z_2 are given by

$$K_j((t, x), (t', x') | \theta_j) = \sigma_j^2 \frac{2^{1-\nu_j}}{\Gamma(\nu_j)} (r_j \sqrt{2\nu_j})^{\nu_j} \mathcal{K}_{\nu_j}(r_j \sqrt{2\nu_j}) + \tau_j^2 \mathbb{1}_{\{t=t', x=x'\}}, \quad (5)$$

for $j \in \{1, 2\}$, where $\mathcal{K}_{\nu_j}(\cdot)$ denotes the modified Bessel function of the second kind with order ν_j (Olver et al., 2010), r_j is the distance between (t, x) and (t', x') defined by

$$r_j^2 = \frac{(t - t')^2}{(\rho_j^t)^2} + \frac{(x - x')^2}{(\rho_j^x)^2}, \quad (6)$$

and $\boldsymbol{\theta}_j = (\sigma_j, \rho_j^t, \rho_j^x, \nu_j, \tau_j)$. τ_j^2 is the variance of the nugget, i.e. we add to the variance at (t, x) an extra variance accounting for the measurement noise. The cross-covariance is given by

$$K_{12}((t, x), (t', x') | \boldsymbol{\theta}_{12}) = \beta \sigma_1 \sigma_2 \frac{2^{1-\nu_{12}}}{\Gamma(\nu_{12})} (r_{12} \sqrt{2\tilde{\nu}_{12}}) \mathcal{K}_{\nu_{12}}(r_{12} \sqrt{2\tilde{\nu}_{12}}) \frac{\sqrt{\rho_1^t \rho_2^t}}{\rho_{12}^t} \frac{\sqrt{\rho_1^x \rho_2^x}}{\rho_{12}^x} \frac{\sqrt{\nu_1 \nu_2}}{\nu_{12}}, \quad (7)$$

where β is the correlation coefficient,

$$\nu_{12} = \frac{\nu_1 + \nu_2}{2}, \quad \tilde{\nu}_{12} = \frac{2\nu_1\nu_2}{\nu_1 + \nu_2}, \quad (\rho_{12}^t)^2 = \frac{\nu_2(\rho_1^t)^2 + \nu_1(\rho_2^t)^2}{\nu_1 + \nu_2}, \quad (\rho_{12}^x)^2 = \frac{\nu_2(\rho_1^x)^2 + \nu_1(\rho_2^x)^2}{\nu_1 + \nu_2}, \quad (8)$$

and

$$r_{12}^2 = \frac{(t - t')^2}{(\rho_{12}^t)^2} + \frac{(x - x')^2}{(\rho_{12}^x)^2}. \quad (9)$$

The parameter vector of the cross-covariance is given by $\boldsymbol{\theta}_{12} = (\beta, \sigma_1, \rho_1^t, \rho_1^x, \nu_1, \sigma_2, \rho_2^t, \rho_2^x, \nu_2)$. The cross-covariance (7) has a similar structure as the marginal (5), and the cross-covariance parameters are all a certain kind of average of their marginal counterparts. For example, $\tilde{\nu}_{12}$ is the harmonic mean of ν_1 and ν_2 , and ρ_{12}^t is a weighted quadratic mean of ρ_1^t and ρ_2^t . It is worth noting that there are several different multivariate Matérn models in the literature, such as (Kleiber & Nychka, 2012) and (Yarger et al., 2024). More generally, half-spectral frameworks (Geoga et al., 2021; Horrell & Stein, 2017; Stein, 2005) can be used to specify significantly broader and more flexible multivariate laws. All of these alternatives could be substituted into this framework with minimal modification, and we elect for the simplest choice here solely for expediency. The most important aspect of this model and application is the weight function $w(t, x)$, which encodes the ABL height. Figure 2 gives an example of a simulated ABL mixture model with parameters chosen to emphasize the transition and dependence structure, demonstrating how this particular design naturally creates sample paths that mimic the true data's sharp transition in local behaviors.

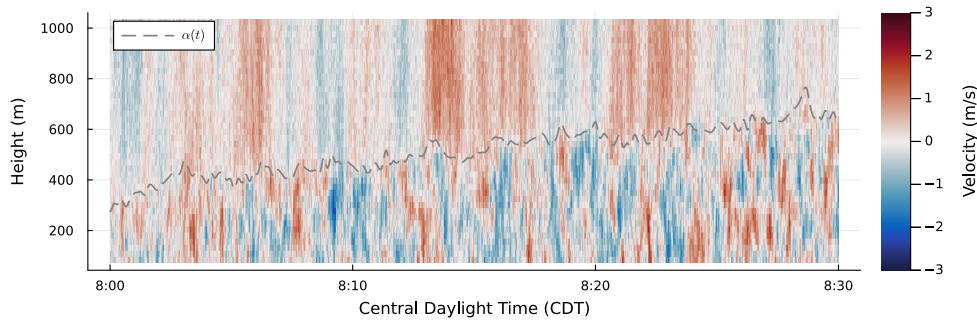


Figure 2: An example of simulated data from the ABL-mixture process given by (2).

Combining (2) with (5) and (7), the marginal covariance function of $Z(t, x)$ is given by

$$\begin{aligned} K((t, x), (t', x') | \boldsymbol{\theta}) = & (1 - w(t, x))(1 - w(t', x'))K_1((t, x), (t', x') | \boldsymbol{\theta}_1) \\ & + w(t, x)w(t', x')K_2((t, x), (t', x') | \boldsymbol{\theta}_2) \\ & + (w(t, x) + w(t', x') - 2w(t, x)w(t', x'))K_{12}((t, x), (t', x') | \boldsymbol{\theta}_{12}), \end{aligned} \quad (10)$$

where $\boldsymbol{\theta}$ contains parameters from K_1, K_2, K_{12} , and $w(t, x)$.

2.3 Fast likelihood approximation: Vecchia’s method

Fast approximation of the Gaussian log-likelihood is an important and widely studied problem in statistics and applied mathematics, and a variety of popular methods have been proposed and analyzed. Broadly speaking, for covariance function-based models these approaches fall into two categories: approximating Σ or approximating $\Omega = \Sigma^{-1}$, often (but not always) using low-rank structure and sparsity respectively. Example approaches that work with Σ include low-rank approximations (Cressie & Johannesson, 2008), tapering-based methods (a rare sparsity-based acceleration in “ Σ -space”) (Kaufman et al., 2008), their combination in the “full-scale approximation” (FSA) (Sang & Huang, 2012), hierarchical matrix approximations that compress off-diagonal blocks (Ambikasaran et al., 2016; Geoga et al., 2020; Litvinenko et al., 2019; Minden et al., 2017), and reduced-operation methods that require only the action $v \mapsto \Sigma v$ (Anitescu et al., 2012; Gardner et al., 2018; Stein et al., 2013; Ubaru et al., 2017), which can then additionally be accelerated with algorithms such as the fast multipole method (FMM) (Greengard & Rokhlin, 1987).

Approximation methods that work directly with $\Omega = \Sigma^{-1}$, on the other hand, are more thematically uniform in that they effectively all make Markovian-like approximations and produce sparse approximations to Ω using arguments of conditional independence. Such approximations have many variations, including Gauss-Markov random fields (Rue & Held, 2005), nearest-neighbor Gaussian processes (Datta et al., 2016; Finley et al., 2019), and Vecchia approximations (Katzfuss & Guinness, 2021; Stein et al., 2004; Vecchia, 1988). In this work, we will use the last term to refer to the approximation.

Vecchia-type approximations are based on a simple idea about approximating conditional distributions. In particular, observing that any joint distribution can be expanded into a product of conditionals as

$$f(y_1, \dots, y_n) = f(y_1) \prod_{j=2}^n f(y_j | y_1, \dots, y_{j-1}), \quad (11)$$

Vecchia (Vecchia, 1988) proposed that for each conditional one could select a subset of prior indices $\sigma(j) \subset [j-1] = \{1, 2, \dots, j-1\}$, typically of size $|\sigma(j)| = \mathcal{O}(1)$, and approximate the true density with

$$f(y_1, \dots, y_n) \approx f(y_1) \prod_{j=2}^n f(y_j | \{y_k : k \in \sigma(j)\}). \quad (12)$$

This simple idea has several very favorable properties: it corresponds to a valid multivariate density, it is embarrassingly parallel to evaluate, and if $|\sigma(j)| = \mathcal{O}(1)$ then the approximation is easily seen

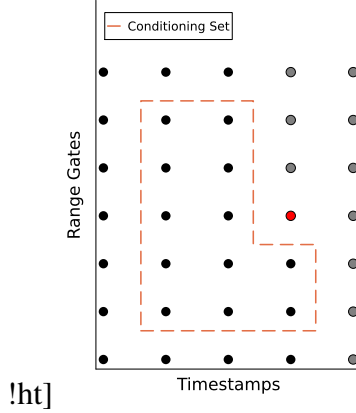


Figure 3: An example of selecting the conditioning set of the red point, where the black points are previous ones, and the gray points have higher indices in the enumeration.

to only require $\mathcal{O}(n)$ work and $\mathcal{O}(1)$ storage to evaluate. This method also has a naturally implied sparse approximation to $\Omega = \Sigma^{-1}$, and we refer readers to (Katzfuss & Guinness, 2021) for details and derivations.

Unlike “ Σ -space” approximation methods that can be made adaptive, however, Vecchia-type approximations are traditionally non-adaptive, and several design choices can significantly impact their accuracy. The first design choice to make is the order in which to enumerate measurements. In one dimension there is a natural ordering to locations based on sorting, but in two or more dimensions there is not a natural or canonical ordering. A second design choice and challenge is that conditioning sets must be selected to specify the approximation before optimizing, and typically stay fixed for the duration of the optimization (with a notable exception being (Kang & Katzfuss, 2023)). For processes with complex dependence structure, it is not always clear how to design and select conditioning sets. Considering that a typical size of $|\sigma(j)|$ is around 10 to keep runtime costs favorable (as runtime costs for each term will grow with the familiar $\mathcal{O}(|\sigma(j)|^3)$), poor choices for conditioning set elements can be very costly in terms of efficiency. With that said, an increasingly large body of work shows Vecchia approximations emerging as a leader in the broad field of approximation methods. For spatial data, theoretically-motivated point ordering and conditioning set selection methods have been proposed that demonstrate favorable performance (Guinness, 2018; Schäfer et al., 2021), and for slowly growing or even fixed conditioning set sizes favorable asymptotic results have also been given (Kang & Katzfuss, 2023; Szabo & Zhu, 2024). Empirically, the approximation can out-compete even much more expensive methods (Heaton et al., 2019).

In this work, however, where the data can effectively be viewed as a vector-valued time series at hundreds of thousands of time points and tens of altitudes, we opt for a simpler design approach than the state-of-the-art in purely spatial data. In particular, we opt for a point ordering that is “space-first”, and we select the conditioning set for measurement y_j based on prior enumerated spatio-temporal nearest neighbors in the intuitive way, as exemplified in Figure 3.

Yet another advantage of Vecchia approximation is that it is much easier than many of its competitors to differentiate. Covariance function-based Gaussian process models are notoriously difficult to fit, as it is commonly the case in fixed-domain asymptotic regimes that only certain nonlinear functions of parameters are consistently estimable and log-likelihood surfaces can exhibit

complex structure that is difficult for optimization routines, particularly derivative-free methods, to navigate (Geoga et al., 2023; Stein et al., 2013). To address this challenge, it is common to optimize using gradients, or ideally both gradients and Hessians (or gradients and expected Fisher information matrices, which can be very effective Hessian approximations (Geoga et al., 2020; Guinness, 2021)). The gradient and Hessian of $\ell(\boldsymbol{\theta})$ are given by

$$\begin{aligned} -2 \frac{\partial}{\partial \theta_j} \ell(\boldsymbol{\theta}) &= \text{tr} \left(\boldsymbol{\Sigma}(\boldsymbol{\theta})^{-1} \boldsymbol{\Sigma}_j(\boldsymbol{\theta}) \right) - \mathbf{y}^T \boldsymbol{\Sigma}(\boldsymbol{\theta})^{-1} \boldsymbol{\Sigma}_j(\boldsymbol{\theta}) \boldsymbol{\Sigma}(\boldsymbol{\theta})^{-1} \mathbf{y}, \\ -2 \frac{\partial^2}{\partial \theta_j \partial \theta_k} \ell(\boldsymbol{\theta}) &= \text{tr} \left(\boldsymbol{\Sigma}(\boldsymbol{\theta})^{-1} \boldsymbol{\Sigma}_j(\boldsymbol{\theta}) \boldsymbol{\Sigma}(\boldsymbol{\theta})^{-1} \boldsymbol{\Sigma}_k(\boldsymbol{\theta}) \right) - \text{tr} \left(\boldsymbol{\Sigma}(\boldsymbol{\theta})^{-1} \boldsymbol{\Sigma}_{jk}(\boldsymbol{\theta}) \right) \\ &\quad + \mathbf{y}^T \left(\frac{\partial}{\partial \theta_k} \left\{ \boldsymbol{\Sigma}(\boldsymbol{\theta})^{-1} \boldsymbol{\Sigma}_j(\boldsymbol{\theta}) \boldsymbol{\Sigma}(\boldsymbol{\theta})^{-1} \right\} \right) \mathbf{y}, \end{aligned} \quad (13)$$

where $\boldsymbol{\Sigma}_j(\boldsymbol{\theta}) = \frac{\partial}{\partial \theta_j} \boldsymbol{\Sigma}(\boldsymbol{\theta})$ and $\boldsymbol{\Sigma}_{jk}(\boldsymbol{\theta}) = \frac{\partial^2}{\partial \theta_j \partial \theta_k} \boldsymbol{\Sigma}(\boldsymbol{\theta})$ are the first and second partial derivative matrices of $\boldsymbol{\Sigma}$ with respect to kernel parameters respectfully. In the case of Vecchia approximations, these precise formulae may be directly applied term-by-term to the log of (12) to obtain the gradient and Hessian respectively. This completely sidesteps the challenge many “ $\boldsymbol{\Sigma}$ -space” methods face of having to compute or approximate large matrix-matrix products involving the (compressed) $n \times n$ matrix $\boldsymbol{\Sigma}$.

As a final small wrinkle, we remark that effective closed-form derivatives of K with respect to all parameters are not available in closed form. Recent work utilizing automatic differentiation (AD) has made estimating the smoothness parameter ν of the Matérn model as easy as any other parameter (Geoga et al., 2023; Griewank & Walther, 2008), and this AD-based approach naturally can be extended to many-parameter models such as this one, making it feasible to rapidly evaluate derivatives and mixed second derivatives of the log-likelihood with respect to even hundreds of distinct parameters. An important but subtle design choice of this model is that parameters pertaining to the weight function $w(t, x)$ or the ABL height function $\alpha(t)$ do not involve derivatives of the covariance functions K_1 , K_2 , or K_{12} , which are by far the most expensive functions in this model to programmatically differentiate, and makes it possible to use reverse-mode AD (as opposed to the forward-mode AD used in differentiating \mathcal{K}_ν in (Geoga et al., 2023)) to more efficiently differentiate with respect to potentially hundreds of parameters in the basis expansion of $\alpha(t)$. While this does not affect the asymptotic cost of the differentiation, the prefactor improvement is significant.

We now discuss the specifics of the estimation problem in detail, noting that the optimal approach for retrieving ABL height varies with the desired temporal and spatial resolution. In the case where one has a reasonably small number of parameters in $\alpha(t)$, say, $m \lesssim 10$, one can simply use jointly optimize over both the ABL and kernel parameters at once in a straightforward way using Vecchia approximations and derivative methods discussed above. In the alternative case where one is interested to obtain a more highly resolved estimate for the ABL height, however, several modifications for scalability are necessary that we will now outline in the next section.

2.4 High-resolution ABL height retrieval

When selecting the family of functions $\{\psi_j\}$ to expand the ABL height function $\alpha(t) = \sum_{j=1}^m c_j \psi_j(t)$ on, several standard options come to mind: splines (Wahba, 1990) are a popular and well-studied tool for function approximation, and so one could pick knot placements and obtain a commensurate number of functions $\{\psi_j(t)\}_{j=1}^m$. One might also consider Chebyshev or some other orthogonal polynomial family (Trefethen, 2019). Both of those choices, and surely many others, are perfectly good ideas, and depending on the application may be the best choice. In the case where m is large, however, a particularly elegant option is to use the domain partitioning and machinery of wavelets (Mallat, 1999), which provide compactly supported and orthogonal functions. By exploiting the dyadic support structure and orthogonality of the shifted and scaled wavelet functions, one can obtain high-quality estimates for $\{c_j\}_{j=1}^m$ for very large m by solving successive optimization problems of constant dimension.

A core concept in wavelet theory is a multiresolution approximation (MRA), which is a sequence $\{V_i\}_{i \in \mathbb{Z}}$ of closed subspaces of $L^2(\mathbb{R})$ indexed by frequency resolution satisfying, among other things, the fact that for $f(t) \in V_i$ one has that (i) translations $f(t - 2^i k)$ are also in V_i and (ii) scalings $f(t/2) \in V_{i+1}$ (see (Mallat, 1999) for a full definition and expository introduction). Oftentimes, MRAs are generated by the scaling and translation of a compactly supported scaling function or mother wavelet, $\psi(x)$, so that $f(t) \in V_i$ is of the form $\psi(2^{-i}t - k)$ for some i and k . Figure 4 shows an example of the Daubechies wavelet of order 8 (Daubechies, 1992) at three increasing levels, with vertical lines indicating the endpoints of support for each individual element in V_i .

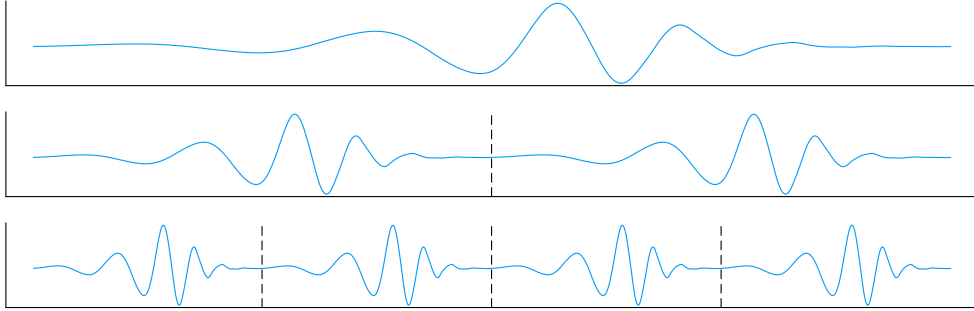


Figure 4: Daubechies wavelets of order 8 at three different resolution levels.

As it pertains to this work, we introduce the following notation. Assuming that we are working with a time segment supported on an interval $[0, 2^I]$, we pick a mother wavelet $\psi(t)$ supported on $[0, 1]$ at level $i = 0$, so that the support of an element in V_I is precisely $[0, 2^I]$. Let that element be denoted $\psi_{I,0}$. In V_{I-1} , then, there will be two elements supported on intervals of length 2^{I-1} that are within $[0, 2^I]$, which we denote $\{\psi_{I-1,0}, \psi_{I-1,1}\}$. Iteratively repeating this process then gives the collection of functions $\{\{\psi_{i,k}\}_{k=0}^{2^{I-i}-1}\}_{i=0}^I$. Using a lexicographic enumeration, we simplify the indexing to give $\{\psi_j\}_{j=1}^m$, where $m = 2^{I+1} - 1$. In this notation, we note that the functions plotted in Figure 4 can be interpreted as ψ_1 in the first row, ψ_2 and ψ_3 in the second, and $\{\psi_j\}_{j=4}^7$ in the third row.

The value in this choice of expanding $\alpha(t) = \sum_{j=1}^m c_j \psi_j(t)$ is that, given fixed covariance

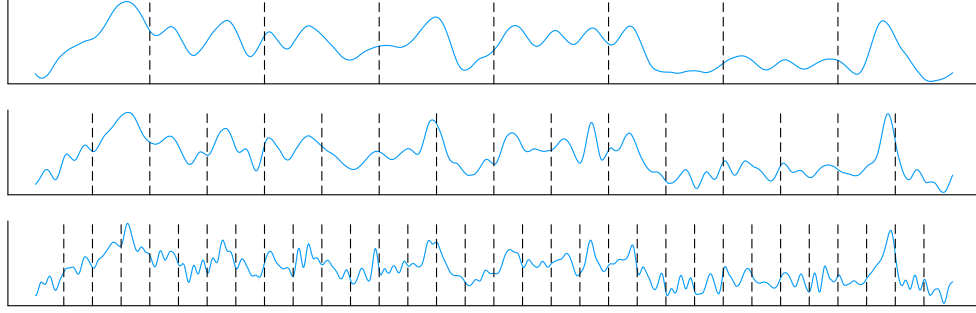


Figure 5: The evolution of a signal with wavelets from low to high frequencies with vertical lines indicating the support of functions ψ_j as the level is decreased.

parameters (which can be estimated in advance in a process that will be detailed in the next section), one can successively refine the estimated function $\alpha(t)$ by decreasing i , and within each level i each parameter can be estimated independently as their supports are disjoint. This refinement like process yields sequentially more highly-resolved estimates of the true ABL height, exemplified with synthetic data in Figure 5. This procedure is summarized in Algorithm 1, with small details like penalizing for $\{c_j\}_{j=1}^m$ and the specifics of initialization omitted for clarity.

```

Data: initial coarse estimate for  $\alpha(t)$ 
Result:  $\alpha(t)$  with optimized wavelet coefficients  $\{\{\hat{c}_{i,k}\}_{k=0}^{2^{I-i}-1}\}_{i=0}^I$ 
// Loop over each wavelet level, starting at the coarsest
for  $i \leftarrow I$  to 0 do
    // Independently fit coefficients for each disjointly supported
     $\psi_{i,k}$ 
    for  $k \leftarrow 0$  to  $2^{I-i} - 1$  do
        // Estimate the coefficient of  $\psi_{i,k}$  by minimizing the negative
        log-likelihood
         $\hat{c}_{i,k} \leftarrow \arg \min -\ell(\alpha(t) + c_{i,k}\psi_{i,k}(t))$ 
        // Update the coefficient of  $\psi_{i,k}$  in  $\alpha(t)$ 
         $\alpha(t) \leftarrow \alpha(t) + \hat{c}_{i,k}\psi_{i,k}(t)$ 
    end
end

```

Algorithm 1: Optimization of wavelet coefficients.

Algorithm 1 updates a single coefficient at each iteration of the inner loop. In this setting, a derivative-free optimization method may be employed to estimate $c_{i,k}$, thereby reducing computational cost by avoiding the evaluation of derivatives and Hessians of the log-likelihood. Alternatively, multiple coefficients may be optimized simultaneously to reduce the total number of inner-loop iterations; however, this approach typically requires derivatives and Hessians to achieve adequate computational efficiency. In practice, one can compare the performance of these strategies and choose the most effective design.

3 Demonstration of ABL height estimation

In this section, we demonstrate the application of the proposed GP framework to the retrieval of ABL height from DL vertical velocity profiles. We present two case studies. First, we illustrate an hour-long, high temporal resolution retrieval to highlight the model’s ability to resolve fine-scale ABL evolution. Second, we examine full-day retrievals under varying meteorological conditions, including periods with cloud contamination where reliable lidar returns are unavailable. We further provide summaries of the covariance function parameters, demonstrating how the model leverages different local properties of the process above and below the ABL height to accurately distinguish between turbulent and non-turbulent regimes across fine timescales. All data analyzed in this section are provided by the Department of Energy’s CROCUS Urban Integrated Field Laboratory project (Collis et al., 2025; Muradyan et al., 2025).

3.1 High-resolution ABL recovery

As an illustrative case, we analyze DL measurements collected from 8 AM to 9 AM (CDT) on July 20, 2023, consisting of vertical velocity observations at 40 range gates with 24-m spacing. Figure 6 shows how the vertical velocity varies with time and height, and the gap at approximately 8:30 AM corresponds to vertical stare measurement interruption as the instrument executes a horizontal scanning sequence to produce a profile of horizontal wind velocities. This morning period is of particular meteorological interest, as surface heating due to solar radiation initiates convective mixing, driving rapid growth of the developing convective boundary layer. Retrieving the ABL height at high temporal resolution involves three key steps: (1) estimating covariance parameters, (2) obtaining an initializer for the ABL height, and (3) successively refining it as described in Section 2.4.

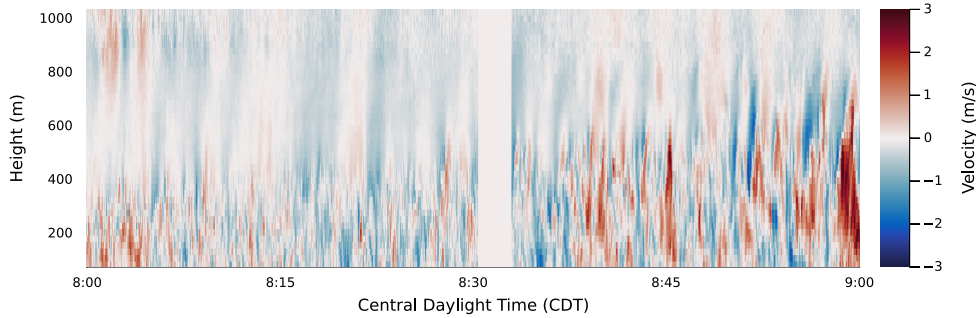


Figure 6: Heatmap of the vertical wind velocity from 8 AM to 9 AM (CDT) on July 20, 2023.

For the first step, covariance parameters of model (2) are estimated using data from subsets of the domain near the lowest and highest altitudes where the instrument SNR exceeds the quality-control threshold (Newsom & Krishnamurthy, 2022). We then fit the bivariate Matérn model of (2) to that data, assuming that these regions are entirely within or above the ABL, such that the weight $w(t, x)$ is either zero or one to effectively machine precision. Figure 7 shows the areas for calculating the MLE of the covariance parameters of Z_1 and Z_2 . The two areas enclosed in black rectangles for the parameters of Z_1 , i.e. $\theta_1 = (\sigma_1, \rho_1^t, \rho_1^x, \nu_1)$, where the nugget variance τ_1 is excluded since

anecdotally with many data segments the optimizer consistently selects it to be zero. The gray boxes indicate data used to determine $\theta_2 = (\sigma_2, \rho_2^t, \rho_2^x, \nu_2, \tau_2)$, the parameters corresponding to the covariance function for Z_2 . Estimated parameter values are summarized in Table 1.

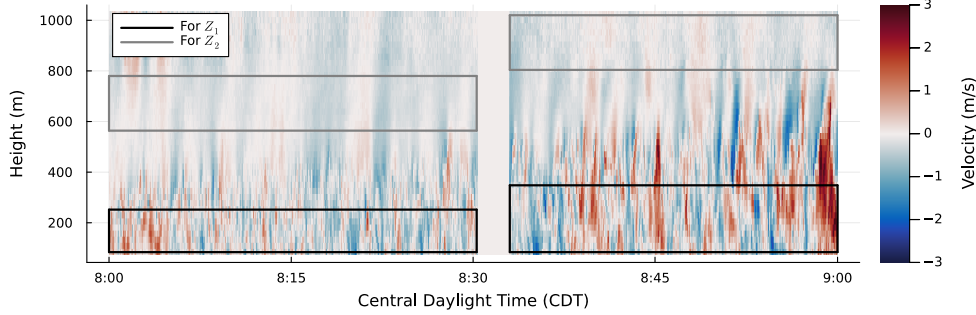


Figure 7: Areas for calculating the MLE of the covariance parameters of Z_1 and Z_2 on July 20, 2023.

Several aspects of these results are worth noting. First and most interestingly, the smoothness parameter ν is estimated to be lower above the ABL than in it, suggesting that the process aloft is modeled as rougher in space and time, contrary to the conventional expectation that turbulent motions within the ABL exhibit greater small-scale variability (Lenschow, 1974; Stull, 2012). This behavior may reflect the limited SNR aloft, which can lead the MLE to attribute additional variability to the process rather than the nugget term. Interestingly, the estimated nugget variance above the ABL of ≈ 0.0025 is smaller than expected, indicating that the optimizer prefers to describe Z_2 as a rough but low-noise process rather than a smooth and noisy one. The remaining parameters follow expected trends: marginal variance and temporal correlation length scale are larger and shorter respectively, for Z_1 , consistent with higher variability and shorter decorrelation times characteristic of the turbulent ABL. The spatial (vertical) correlation above the ABL is more pronounced, reflecting the smoother, more coherent flow typical of the free atmosphere.

With $\hat{\theta}_1$ and $\hat{\theta}_2$, we now fit a coarse spline basis with eight knots, again using the log-likelihood, to initialize the ABL height. Successive refinements of this spline-based initializer are then computed. The results of multiple levels of refinement are summarized in Figure 8. The dashed gray line in each subplot shows the spline-based initializer. The solid black line is the estimated ABL height using Daubechies wavelets, which in each row of Figure 8 adds two finer levels of resolution, totaling to $m = 384$ wavelets in the final figure. With each refinement, this spline estimator can be observed to accurately capture new fine scale features: moving from the first panel to the second, for example, we note that the dip in ABL height at approximately 8:35 AM is captured, and that moving from the second to the third panel several sharp gusts—such as at approximately 8:25 and 8:50 AM—are now captured.

3.2 Full-day ABL profiles

In this section, we reduce the temporal resolution of the ABL height retrieval function $\alpha(t)$ to produce full-day profiles that capture the complete diurnal cycle. The key additional challenge in this setting is that the process is not stationary in time, as the underlying turbulence, stability, and aerosol structure of the ABL vary systematically with progression from the convective boundary

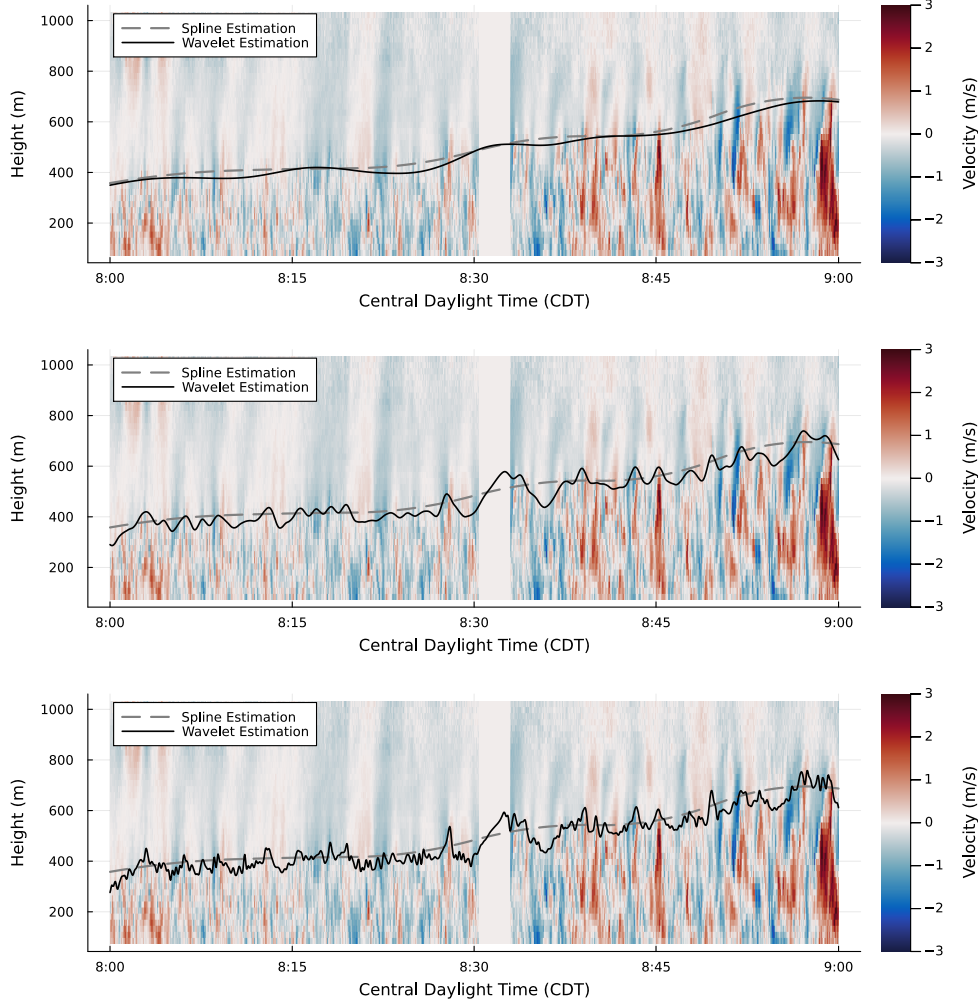


Figure 8: The ABL height estimation using wavelets on July 20, 2023 using increasingly fine wavelet resolutions for the expansion of $\alpha(t)$. In all panels, the spline initializer is shown in grey.

layer to the stable nocturnal layer (Garratt, 1994; Mahrt, 2014; Stull, 2012). As a result, the covariance parameters θ must be re-estimated adaptively as the time of day changes. This estimation procedure largely follows the high-resolution case described in the previous section, with several important modifications. First, a temporal smoothness constraint implemented as a small continuity penalty at the endpoints of consecutive hourly segments is applied to ensure piecewise estimates for $\alpha(t)$ remain continuous across the full 24-hour period. Second, the covariance parameters are reinitialized each hour using the in- or above-ABL process parameters inferred from the preceding hour. This allows the model to adapt to gradual diurnal evolution in stability and turbulence intensity.

We analyze three days with distinct meteorological conditions and cloud regimes. For each day, data are available from 6 AM to 9 PM local time, spanning the full period from morning transition to evening stabilization. For each hour, we use a simple linear function as the initial guess and six quadratic splines to estimate the ABL height. After concatenating all hourly fits, we

use 60 quadratic splines to smooth the contact points of the ABL height of different hours. Figure 9 summarizes the estimated ABL height for these three days, selected to exhibit different patterns of data availability and atmospheric variability.

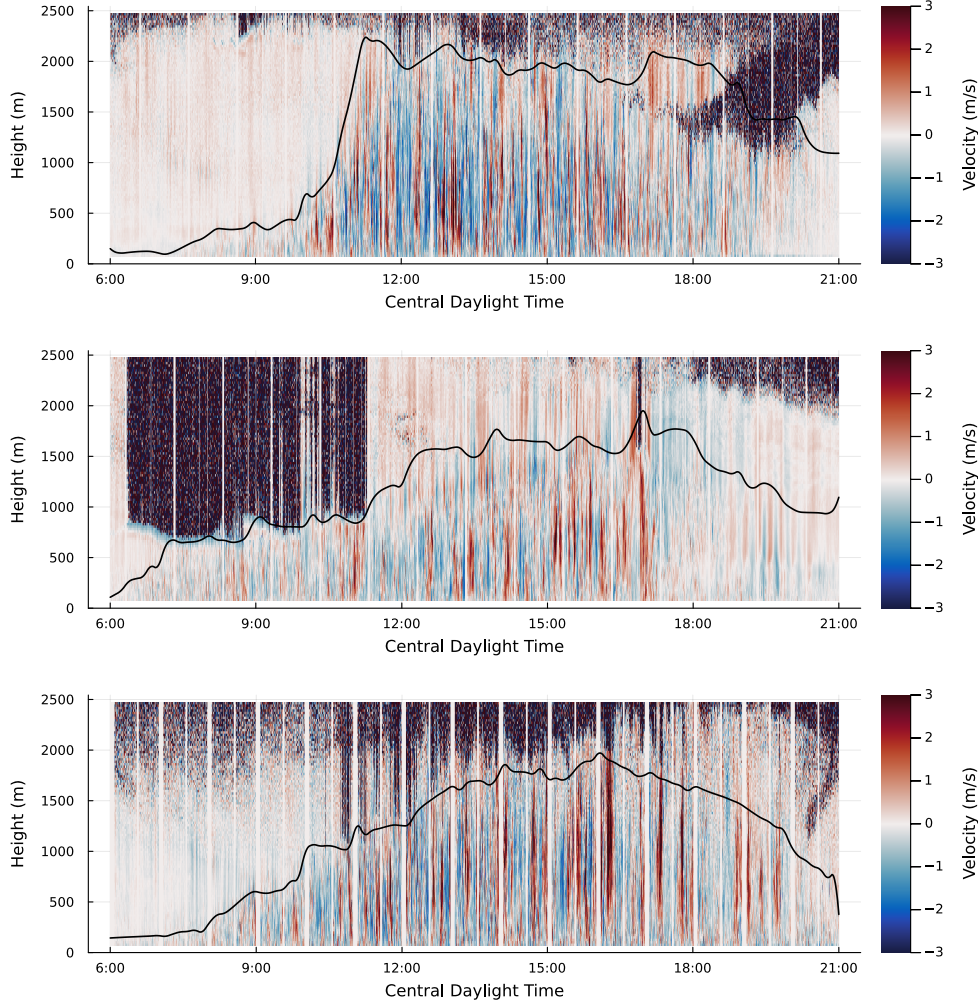


Figure 9: The ABL height estimation using splines on June 23, 2023 (top row), June 27, 2023 (middle row), and July 20 (bottom row).

As Figure 9 demonstrates, the diurnal evolution of the ABL height is captured realistically across diverse meteorological conditions, including periods of missing or low-SNR data and transitions between convective, residual and stable regimes. The three examples exhibit distinct temporal correlation structures: June 27 (middle panel) displays the longest dependence scales and smoothest ABL height growth, consistent with weaker convective forcing and intermittent cloud shading (clouds between 6:15 and 11:40 AM), whereas July 20 (bottom panel) shows strong short-term variability and enhanced turbulence intermittency, indicative of vigorous convective mixing likely under clear-sky, high insolation conditions. In contrast, June 23 (top panel) represents a more transitional case, characterized by a well-defined growth phase followed by gradual afternoon stabilization. On July 20, the ABL remains deep and coherent throughout most of the day,

reflecting persistent surface heating and sustained convective overturning, with the ABL height oscillations after local noon likely associated with entrainment-zone variability and thermal plume organization rather than retrieval noise. These examples collectively highlight that the proposed GP retrieval framework performs robustly across a range of atmospheric states, maintaining physically consistent ABL height estimates even under strong turbulence, partial cloud cover, or transient data gaps. Moreover, the differences among the three days underscore that different covariance features (e.g., marginal variance, temporal correlation length, or nugget variance) can dominate as discriminants between in- and above-ABL regimes, depending on the prevailing meteorological forcing and turbulence intensity.

Finally, it is worth noting that because the proposed model is globally nonstationary in time but locally stationary within short intervals, it naturally adapts to the diurnal transition between boundary layer regimes. The mixture model for $Z(t, x)$, representing distinct dynamic behaviors in and above the ABL, allows the same framework to continuously transition from the convective daytime boundary layer to the stable nocturnal boundary layer (NBL) without any explicit change in model structure or thresholds. This capability is particularly valuable, as retrieving the NBL height remains a persistent challenge for traditional variance-threshold or gradient-based methods, owing to the weaker turbulence, smaller vertical gradients, and reduced contrast between sub- and super-layer properties at night (Mahrt, 2014; Van de Wiel et al., 2012). By capturing these gradual transitions through time-varying covariance parameters, the GP approach provides a physically consistent and automated means of identifying both convective and stable boundary-layer regimes within a single probabilistic framework.

4 Discussion

High temporal resolution retrievals of the ABL height offer significant advances for both scientific understanding and operational applications. The ABL height as a function of time characterizes the dynamic boundary between the surface and the free atmosphere. Traditional hourly estimates can miss the rapid fluctuations of this boundary, particularly during morning growth, evening collapse, or episodic events such as lake breezes, convection bursts, or frontal passages, when changes can occur on timescales of minutes. Resolving these short-term fluctuations enables better quantification of entrainment processes at the top of the boundary layer, improved closure of energy and mass budgets, and more accurate representation of turbulence intermittency. For researchers, such fine-scale ABL height observations provide essential validation targets for high-resolution models, large-eddy simulations, and land-atmosphere coupling studies. Operational forecasters, regulatory and environmental agencies such as the National Weather Service and the U.S. Environmental Protection Agency, as well as energy and transportation sectors, can all benefit from rapid updates in boundary-layer depth. Such information improves real-time assessments of surface pollutant concentrations, plume dispersion, fog and low-cloud formation, and the timing of convection initiation. Beyond the research community, urban planners, public-health officials, and emergency-response organizations can also leverage these data for exposure risk evaluation, smoke and hazardous-release dispersion modeling, near-surface temperature and humidity forecasting, and applications where the difference between a one-minute and one-hour temporal resolution can critically influence operational decisions and public-safety outcomes.

In this study, we introduced a method for using purpose-built Gaussian process models to identify the height of the atmospheric boundary layer using both marginal- and cross-covariance structure of the process within and above it. Unlike prior work in this area (Geoga et al., 2021), this method allows a fully varying ABL height $\alpha(t)$ and can be used to obtain extremely high-resolution estimates for the time-varying process. With that said, however, many important statistical questions remain: a more careful analysis of the appropriate level of shrinkage used to avoid introducing spurious fluctuations in $\alpha(t)$ would be valuable, and a more flexible model for the marginal- and cross-dependence structure of the Z_1 and Z_2 processes may result in better estimates. Further, the model requires having some data both within and above the ABL, and thus it is not viable in situations such as calm, stable nights when the nocturnal ABL becomes too shallow to be sampled. These questions and many application-based enhancements are exciting questions for future work.

References

- Ambikasaran, S., Foreman-Mackey, D., Greengard, L., Hogg, D., & O’Neil, M. (2016). Fast direct methods for Gaussian processes. *IEEE Transactions on Pattern Analysis and Machine Intelligence*, 38(2), 252–265. <https://doi.org/10.1109/TPAMI.2015.2448083>
- Anitescu, M., Chen, J., & Wang, L. (2012). A matrix-free approach for solving the parametric Gaussian process maximum likelihood problem. *SIAM Journal on Scientific Computing*, 34(1), A240–A262.
- Baklanov, A., Schlünzen, K., Suppan, P., Baldasano, J., Brunner, D., Aksoyoglu, S., Carmichael, G., Douros, J., Flemming, J., Forkel, R., et al. (2014). Online coupled regional meteorology chemistry models in europe: Current status and prospects. *Atmospheric Chemistry and Physics*, 14(1), 317–398.
- Collis, S., Muradyan, P., Jackson, R., Raut, B. A., O’Brien, J. R., Tuftedal, M. E., Grover, M. A., Kotamarthi, V. R., Negri, M. C., Fytanidis, D. K., Hence, D. A., Nesbitt, S. W., Weart, B., Pal, S., Wawrzyniak, E., Piot, J., Wagner, T. J., Sherman, Z., Wu, S., . . . Beaudry, S. (2025). Crocus urban canyons: Observing and modeling boundary layer structure and processes in a complex urban environment [Manuscript submitted for publication, September 2025]. *Bulletin of the American Meteorological Society*.
- Cressie, N., & Johannesson, G. (2008). Fixed rank Kriging for very large spatial data sets. *Journal of the Royal Statistical Society: Series B (Statistical Methodology)*, 70(1), 209–226.
- Dabberdt, W. F., Carroll, M. A., Baumgardner, D., Carmichael, G., Cohen, R., Dye, T., Ellis, J., Grell, G., Grimmond, S., Hanna, S., et al. (2004). Meteorological research needs for improved air quality forecasting: Report of the 11th prospectus development team of the us weather research program. *Bulletin of the American Meteorological Society*, 85(4), 563–586.
- Dang, R., Yang, Y., Li, H., Hu, X., Wang, Z., Huang, Z., Zhou, T., & Zhang, T. (2019). Atmosphere boundary layer height (ablh) determination under multiple-layer conditions using micro-pulse lidar. *Remote Sensing*, 11(3), 263.
- Datta, A., Banerjee, S., Finley, A., & Gelfand, A. (2016). Hierarchical nearest-neighbor gaussian process models for large geostatistical datasets. *Journal of the American Statistical Association*, 111(514), 800–812.

- Daubechies, I. (1992). *Ten lectures on wavelets*. SIAM.
- Eresmaa, N., Karppinen, A., Joffre, S., Räsänen, J., & Talvitie, H. (2006). Mixing height determination by ceilometer. *Atmospheric Chemistry and Physics*, 6(6), 1485–1493.
- Finley, A., Datta, A., Cook, B., Morton, D., Andersen, H., & Banerjee, S. (2019). Efficient algorithms for bayesian nearest neighbor gaussian processes. *Journal of Computational and Graphical Statistics*, 28(2), 401–414.
- Fuentes, M., & Smith, R. (2001). *A new class of nonstationary models* (tech. rep.). Tech. report at North Carolina State University, Institute of Statistics.
- Gardner, J., Pleiss, G., Weinberger, K., Bindel, D., & Wilson, A. (2018). Gpytorch: Blackbox matrix-matrix gaussian process inference with gpu acceleration. *Advances in neural information processing systems*, 31.
- Garratt, J. R. (1994). The atmospheric boundary layer. *Earth-Science Reviews*, 37(1-2), 89–134.
- Geoga, C. J., Marin, O., Schanen, M., & Stein, M. L. (2023). Fitting matérn smoothness parameters using automatic differentiation. *Statistics and Computing*, 33(2), 48.
- Geoga, C., Anitescu, M., & Stein, M. (2020). Scalable Gaussian process computations using hierarchical matrices. *Journal of Computational and Graphical Statistics*, 29(2), 227–237. <https://doi.org/10.1080/10618600.2019.1652616>
- Geoga, C., Anitescu, M., & Stein, M. (2021). Flexible nonstationary spatiotemporal modeling of high-frequency monitoring data. *Environmetrics*, 32(5). <https://doi.org/10.1002/env.2670>
- Gneiting, T., Kleiber, W., & Schlather, M. (2010). Matérn cross-covariance functions for multivariate random fields. *Journal of the American Statistical Association*, 105(491), 1167–1177. <https://doi.org/10.1198/jasa.2010.tm09420>
- Greengard, L., & Rokhlin, V. (1987). A fast algorithm for particle simulations. *Journal of computational physics*, 73(2), 325–348.
- Griewank, A., & Walther, A. (2008). *Evaluating derivatives: Principles and techniques of algorithmic differentiation*. SIAM.
- Guinness, J. (2018). Permutation and grouping methods for sharpening Gaussian process approximations. *Technometrics*, 60(4), 415–429. <https://doi.org/10.1080/00401706.2018.1437476>
- Guinness, J. (2021). Gaussian process learning via fisher scoring of vecchia’s approximation. *Statistics and Computing*, 31(3), 25.
- Heaton, M. J., Datta, A., Finley, A. O., Furrer, R., Guinness, J., Guhaniyogi, R., Gerber, F., Gramacy, R. B., Hammerling, D., Katzfuss, M., Lindgren, F., Nychka, D. W., Sun, F., & Zammit-Mangion, A. (2019). A Case Study Competition Among Methods for Analyzing Large Spatial Data. *Journal of Agricultural, Biological and Environmental Statistics*, 24(3), 398–425. <https://doi.org/10.1007/s13253-018-00348-w>
- Holtslag, A., & Boville, B. (1993). Local versus nonlocal boundary-layer diffusion in a global climate model. *Journal of climate*, 6(10), 1825–1842.
- Holtslag, A., Svensson, G., Baas, P., Basu, S., Beare, B., Beljaars, A., Bosveld, F., Cuxart, J., Lindvall, J., Steeneveld, G., et al. (2013). Stable atmospheric boundary layers and diurnal cycles: Challenges for weather and climate models. *Bulletin of the American Meteorological Society*, 94(11), 1691–1706.
- Horrell, M., & Stein, M. (2017). Half-spectral space–time covariance models. *Spatial Statistics*, 19, 90–100. <https://doi.org/10.1016/j.spasta.2016.12.002>

- Kang, M., & Katzfuss, M. (2023). Correlation-based sparse inverse cholesky factorization for fast gaussian-process inference. *Statistics and Computing*, 33(3). <https://doi.org/10.1007/s11222-023-10231-5>
- Katzfuss, M., & Guinness, J. (2021). A general framework for Vecchia approximations of Gaussian processes. *Statistical Science*, 36(1), 124–141.
- Kaufman, C., Schervish, M., & Nychka, D. (2008). Covariance tapering for likelihood-based estimation in large spatial data sets. *Journal of the American Statistical Association*, 103(484), 1545–1555.
- Kleiber, W., & Nychka, D. (2012). Nonstationary modeling for multivariate spatial processes. *Journal of Multivariate Analysis*, 112, 76–91. [https://doi.org/https://doi.org/10.1016/j.jmva.2012.05.011](https://doi.org/10.1016/j.jmva.2012.05.011)
- Kotthaus, S., Haefelin, M., Drouin, M., Dupont, J., Grimmond, S., Haefele, A., Hervo, M., Poltera, Y., & Wiegner, M. (2020). Tailored algorithms for the detection of the atmospheric boundary layer height from common automatic lidars and ceilometers (alc). *Remote Sensing*, 12(19), 3259.
- Lenschow, D. (1974). Model of the height variation of the turbulence kinetic energy budget in the unstable planetary boundary layer. *Journal of Atmospheric Sciences*, 31(2), 465–474.
- Litvinenko, A., Sun, Y., Genton, M., & Keyes, D. (2019). Likelihood approximation with hierarchical matrices for large spatial datasets. *Computational Statistics & Data Analysis*, 137, 115–132. <https://doi.org/10.1016/j.csda.2019.02.002>
- Mahrt, L. (2014). Stably stratified atmospheric boundary layers. *Annual review of fluid mechanics*, 46(1), 23–45.
- Mallat, S. (1999). *A wavelet tour of signal processing*. Elsevier.
- Minden, V., Damle, A., Ho, K. L., & Ying, L. (2017). Fast spatial gaussian process maximum likelihood estimation via skeletonization factorizations. *Multiscale Modeling & Simulation*, 15(4), 1584–1611.
- Muradyan, P., Collis, S., O’Brien, J. R., Grover, M., Jackson, R., Tuftedal, M., Wawrzyniak, E., Negri, C., Vincent, A. E. S., Park, S. Y., Miller, W. M., Nesbitt, S., Wagner, T., Pal, S., Berkelhammer, M., Gonzalez-Meler, M., Cho, A., Lee, J., & McNicol, G. (2025). Crocus micronet: An ai-enabled, multi-tier urban observation system for weather-driven resilience in chicago [Manuscript submitted for publication, December 2025]. *Bulletin of the American Meteorological Society*.
- Newsom, R., & Krishnamurthy, R. (2022). *Doppler lidar (dl) instrument handbook* (tech. rep.). DOE Office of Science Atmospheric Radiation Measurement (ARM) User Facility.
- Olver, F., Lozier, D., Boisvert, R., & Clark, C. (2010). *Nist handbook of mathematical functions*. Cambridge university press.
- Pearson, G., Davies, F., & Collier, C. (2009). An analysis of the performance of the ufam pulsed doppler lidar for observing the boundary layer. *Journal of Atmospheric and Oceanic Technology*, 26(2), 240–250.
- Rue, H., & Held, L. (2005). *Gaussian markov random fields: Theory and applications*. Chapman; Hall/CRC.

- Sang, H., & Huang, J. (2012). A full scale approximation of covariance functions for large spatial data sets. *Journal of the Royal Statistical Society Series B: Statistical Methodology*, 74(1), 111–132.
- Schäfer, F., Katzfuss, M., & Owhadi, H. (2021). Sparse cholesky factorization by Kullback–Leibler minimization. *SIAM Journal on Scientific Computing*, 43(3), A2019–A2046. <https://doi.org/10.1137/20M1336254>
- Stein, M. L. (1999, June). *Interpolation of spatial data: Some theory for kriging*. Springer Science & Business Media.
- Stein, M. (2005). Statistical methods for regular monitoring data. *Journal of the Royal Statistical Society: Series B (Statistical Methodology)*, 67(5), 667–687. <https://doi.org/10.1111/j.1467-9868.2005.00520.x>
- Stein, M., Chen, J., & Anitescu, M. (2013). Stochastic approximation of score functions for Gaussian processes. *The Annals of Applied Statistics*, 7(2), 1162–1191. <https://doi.org/10.1214/13-AOAS627>
- Stein, M., Chi, Z., & Welty, L. (2004). Approximating likelihoods for large spatial data sets. *Journal of the Royal Statistical Society: Series B (Statistical Methodology)*, 66(2), 275–296.
- Stull, R. B. (2012). *An introduction to boundary layer meteorology* (Vol. 13). Springer Science & Business Media.
- Szabo, B., & Zhu, Y. (2024). Vecchia gaussian processes: Probabilistic properties, minimax rates and methodological developments. *arXiv preprint arXiv:2410.10649*.
- Trefethen, L. N. (2019). *Approximation theory and approximation practice, extended edition*. SIAM.
- Tucker, S., Senff, C., Weickmann, A., Brewer, W. A., Banta, R., Sandberg, S., Law, D., & Hardesty, R. M. (2009). Doppler lidar estimation of mixing height using turbulence, shear, and aerosol profiles. *Journal of Atmospheric and Oceanic Technology*, 26(4), 673–688. <https://doi.org/10.1175/2008JTECHA1157.1>
- Ubaru, S., Chen, J., & Saad, Y. (2017). Fast estimation of $\text{tr}(f(a))$ via stochastic lanczos quadrature. *SIAM Journal on Matrix Analysis and Applications*, 38(4), 1075–1099.
- Van de Wiel, B., Moene, A., & Jonker, H. (2012). The cessation of continuous turbulence as precursor of the very stable nocturnal boundary layer. *Journal of the Atmospheric Sciences*, 69(11), 3097–3115.
- Vecchia, A. (1988). Estimation and model identification for continuous spatial processes. *Journal of the Royal Statistical Society: Series B (Methodological)*, 50(2), 297–312.
- Wahba, G. (1990). *Spline models for observational data*. SIAM.
- Wang, F., Yang, T., Wang, Z., Chen, X., Wang, H., & Guo, J. (2021). A comprehensive evaluation of planetary boundary layer height retrieval techniques using lidar data under different pollution scenarios. *Atmospheric Research*, 253, 105483.
- Wang, Y., Wang, S., Lewis, J., Chang, S., & Griffith, S. (2021). Determining planetary boundary layer height by micro-pulse lidar with validation by uav measurements. *Aerosol and Air Quality Research*, 21(5), 200336.
- Yarger, D., Stoev, S., & Hsing, T. (2024). Multivariate matérn models – a spectral approach. <https://arxiv.org/abs/2309.02584>

GP	$\hat{\sigma}$	$\hat{\rho}^t$	$\hat{\rho}^x$	$\hat{\nu}$	$\hat{\tau}$
Z_1	6.64e-1 (9.59e-3)	2.62 (4.69e-2)	9.12e1 (1.38)	1.52 (1.44e-2)	
Z_2	4.30e-1 (1.08e-1)	1.45e2 (5.79e1)	1.24e3 (5.02e2)	7.91e-1 (3.21e-2)	5.50e-2 (2.18e-4)

Table 1: The MLE of parameters of Z_1 and Z_2 based on Figure 7 with standard deviations provided in parentheses.